Supplementary Material

Spectroscopic investigations under whole cell conditions provide new insight into the metal hydride chemistry of [FeFe]-hydrogenase

Lívia S. Mészáros[a], ‡, Pierre Ceccaldi[a], ‡, Marco Lorenzi[a], Holly J. Redman[a], Emanuel Pfitzner[b], Joachim Heberle[b], Moritz Senger[b], Sven T. Stripp[b]* and Gustav Berggren[a]*

[a] L. S. Mészáros, P. Ceccaldi, M. Lorenzi, H. J. Redman, G. Berggren; Molecular Biomimetics, Dept. of Chemistry – Ångström Laboratory; Uppsala University; Lägerhyddsvägen 1, SE-75120, Uppsala, Sweden

[b] E. Pfitzner, J. Heberle, M. Senger, S. T. Stripp; Institute of Experimental Physics, Experimental Molecular Biophysics; Freie Universität Berlin; Arnimallee 14, DE-14195, Berlin, Germany

‡ These authors contributed equally

* E-mail: sven.stripp@fu-berlin.de and gustav.berggren@kemi.uu.se

Table of contents

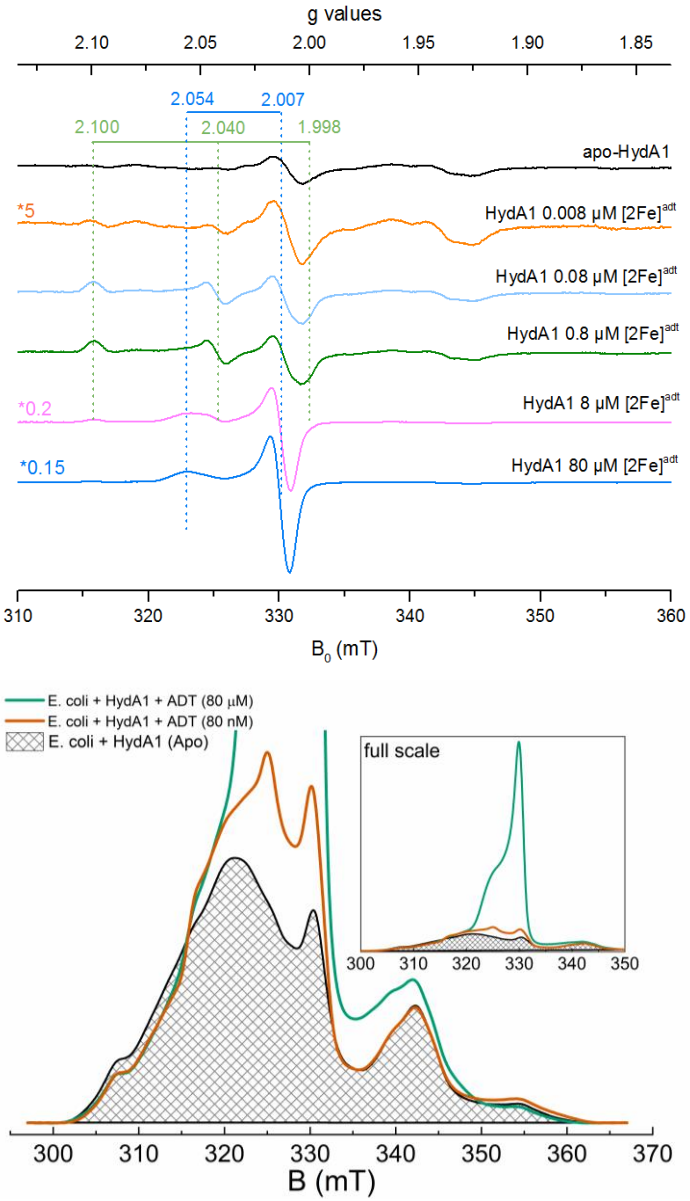

Figure S1. ***In vivo*** **H-cluster assembly monitored using X-band EPR spectroscopy**.

(**Top**) Non-background subtracted whole-cell EPR spectra recorded on *E. coli* cells expressing apo-HydA1. Samples collected from cells incubated in the absence (apo-HydA1) and presence of 0.008 – 80 µM $[2Fe]^{adt}$, as described for Figure 2 (main text). The spectra are shown with a wider scan window following baseline correction but without background subtraction. EPR spectra were recorded at 20 K, 1 mW microwave power, at a microwave frequency of 9.28 GHz. g-values of H_{ox} and H_{ox}-CO indicated in green and blue, respectively.

(**Bottom**) Selected integrated whole-cell EPR spectra recorded on cells incubated in the absence (apo-HydA1, black, hashed area) and presence of 0.08 µM (orange) or 80 µM (green) $[2Fe]^{adt}$ shown for comparative purposes. At lower $[2Fe]^{adt}$ the background signals dominate over signals attributed to the H-cluster, while the converse is observed at higher $[2Fe]^{adt}$ concentrations (i.e. 8-80 µM). This results in a significant uncertainty in the spin quantification at early titration points, in addition to the estimated error from the simulation and comparison to the Cu standard. The spectra were recorded as described in Figure S1A and baseline corrected but not background subtracted.

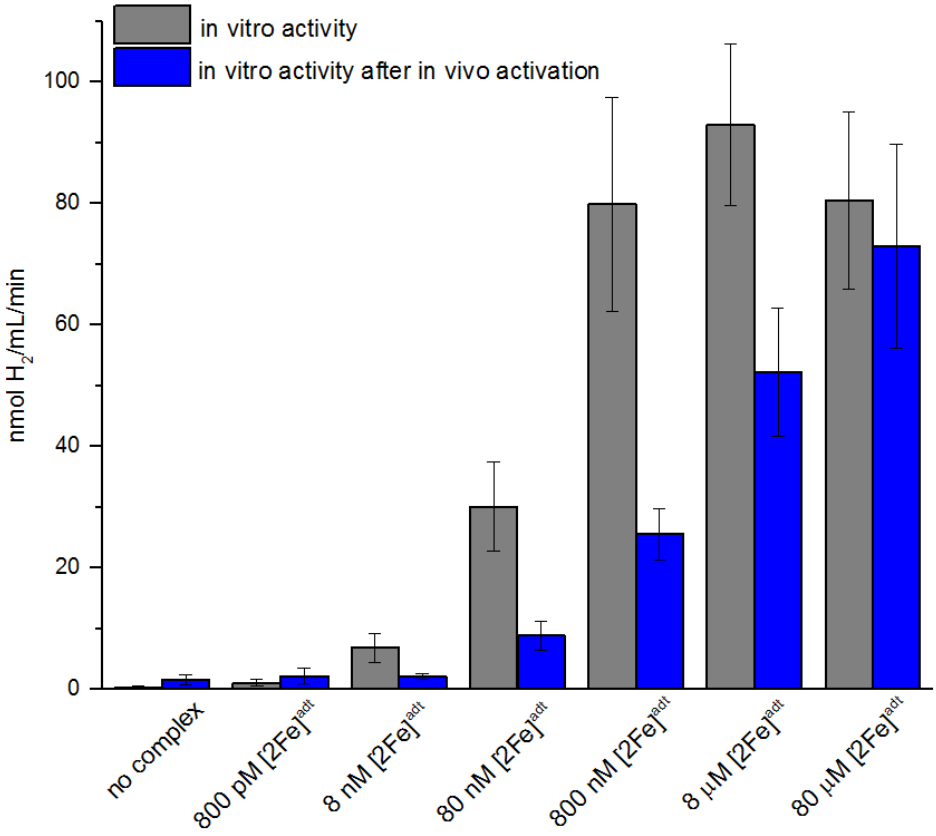

Figure S2. Extent of activation determined through *in vitro* enzymatic H_2 release assays.

The fraction of available apo-HydA1 activated *in vivo* was determined using standard enzymatic assays, by comparing the maximum activity observed for enzymes activated either *in vivo* or *in vitro* as previously described.[1] The total amount of apo-HydA1 available for activation was determined through *in vitro* activation assays. Cultures were prepared in an identical fashion to the EPR sample preparation protocol, but lysed prior to addition of the cofactor. Under such *in vitro* conditions, activation of apo-HydA1 is expected to proceed quantitatively and the resulting hydrogenase activity was determined in standard methyl viologen/dithionite assays (grey bars).[2] This *in vitro* activation protocol resulted in a maximum H_2 production rate of 93.0 (± 14%) nmol $H_2 \cdot min^{-1} \cdot mL^{-1}$, reached after addition of 1-10 µg $[2Fe]^{adt}$ (0.8-8 µM final concentration). In parallel, apo-HydA1 expressing cells were treated with varying amounts of the synthetic cofactor analogously to the EPR sample preparation protocol, washed and lyzed into KPi buffer as previously described.[1] Following this *in vivo* activation a maximum activity of 73.0 (± 23%) nmol H_2 min^{-1} mL^{-1} was reached, after addition of 100 µg $[2Fe]^{adt}$ (80 µM final concentration) (blue bars). In combination, the enzymatic assays reveal a high degree of activation of the enzyme also under *in vivo* conditions (approx. 80% of total enzyme content) albeit with a requirement for larger excess of the synthetic cofactor as compared to the *in vitro* protocol.

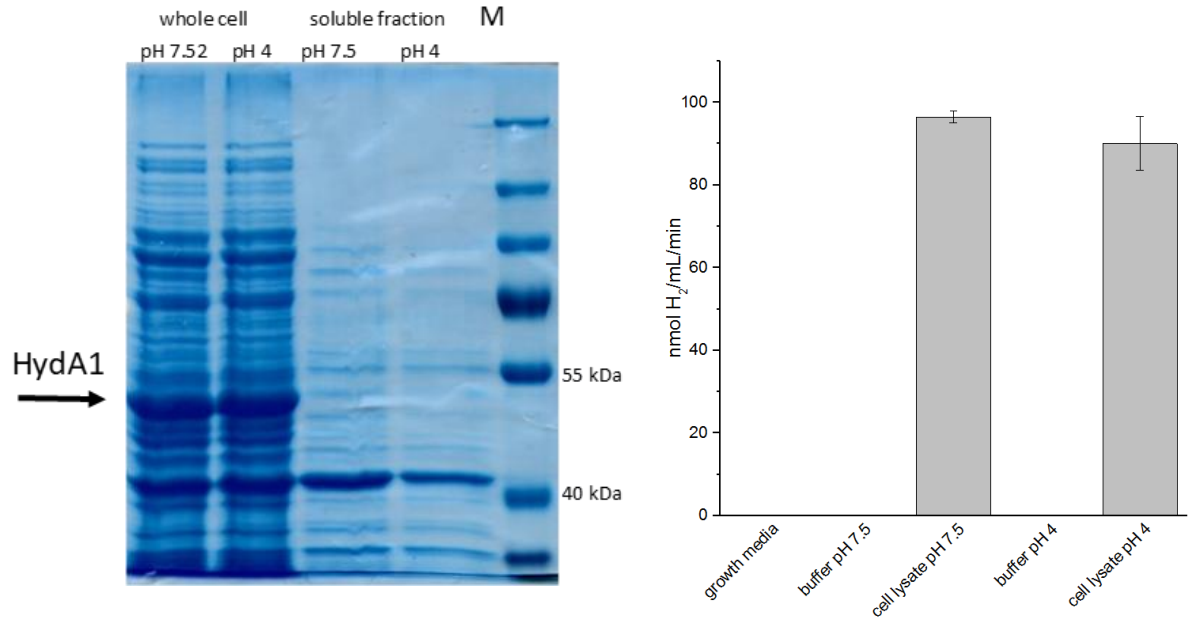

Figure S3. Cellular integrity and localization of the hydrogenase protein at pH 7.5 and 4.

(**Left**) **SDS page gel analysis.** [2Fe]^{adt}-HydA1 containing cells were incubated in TRIS-HCl buffer at pH 7.5 and at pH 4 respectively for 30 minutes. In the case of pH 4 medium, the TRIS-HCl buffer was acidified by HCl addition and the pH stability verified after the 1 h incubation. Then the cells were separated from the buffer with high-speed centrifugation. The whole-cell samples and the soluble fractions were analyzed in 1:1 ratio using 10% SDS-PAGE gel. (M): PageRuler Prestained Protein Ladder (Thermo Fisher Scientific) as reference. No distinct difference in cell lysis was observed between acidic and weakly alkaline medium. Additionally, growing the cells on ampicillin containing LB-agar plates, the pH 4 incubated cells showed growth comparable to cells in pH 7.5 medium, in agreement with other reports on the acid stability of *E. coli*. [3]

(Right) ***In vitro*** **enzyme assays.** To ensure that the hydrogenase enzyme is located inside the cells regardless of pH during incubation, *in vitro* activity assays were performed. 50 mL cell cultures overproducing apo-HydA1 were prepared as described in the methods section. Following the over-expression, the cell paste was separated from the growth media through centrifugation. The supernatant was stored for assays (growth media), while the resulting cell paste was washed three times by re-suspending them in 1 mL TRIS-HCl buffer pH 7.5 (100 mM TRIS, 150 mM NaCl), before they were incubated in 1 mL pH 7.5 or pH 4 TRIS-HCl media under anaerobic conditions. After 30 min the cell paste was again separated from the media through centrifugation. The resulting supernatants were kept for assays (buffer pH 7.5 and pH 4), while the cells were lysed to solubilize the cell contents (cell lysate pH 7.5 and pH 4). Aliquots of the generated samples were treated with 80 µM [2Fe]^{adt} to activate any apo-HydA1 in the different fractions. *In vitro* enzymatic assays were then performed on the cell-free growth media, on the pH 7.5 and pH 4 TRIS-HCl media after separation from the cells, and on the cell-lysates; as previously described.[1] As seen in Figure S3 (right), hydrogenase activity was only observed in the cell lysate fractions.

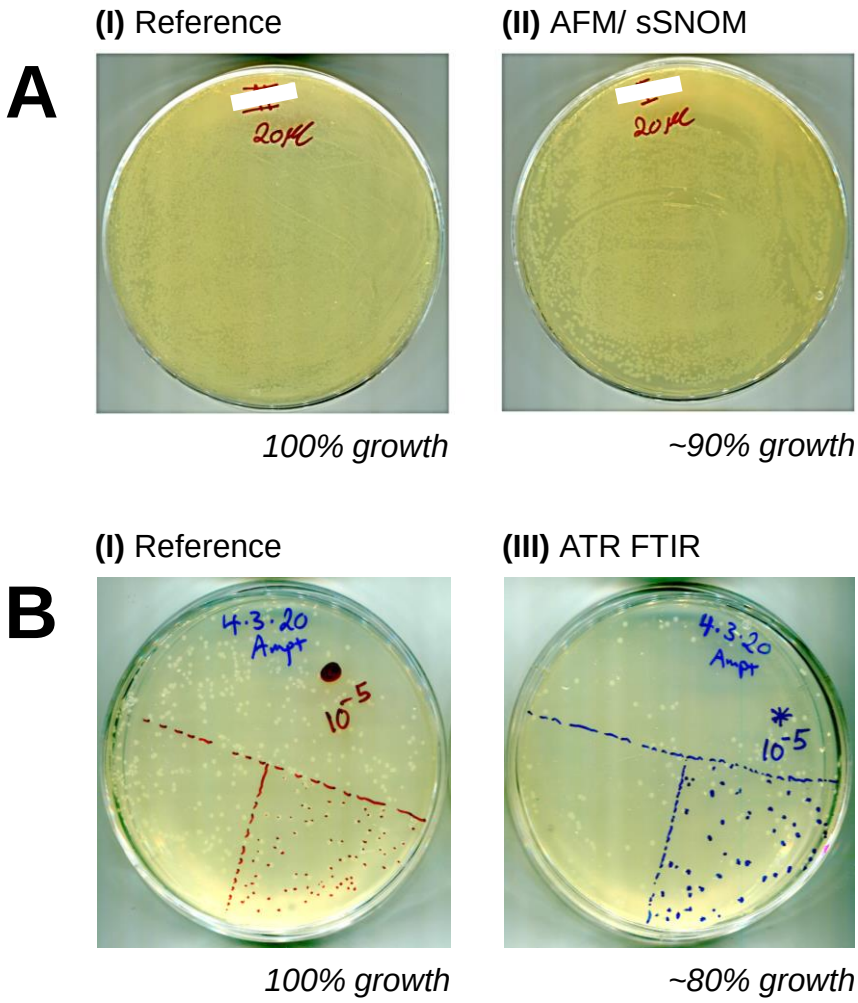

Figure S4. Viability of *E. coli* cells under different experimental conditions.

To probe whether recombinant *E. coli* cells not only retain their structural integrity, but also remain viable during the different modes of sample preparation, three experiments were performed. **(I)** Reference conditions. 1 µL cell culture was kept at room temperature for 60 min (liquid sample, *i.e.* as in EPR experiments, no film formation). **(II)** AFM/ sSNOM conditions. 1 µL standard cell culture was pipetted on the silicon crystal of the ATR cell and kept under dry N_2 (duration: 60 min). **(III)** ATR FTIR conditions. 1 µL cell culture was pipetted on the silicon crystal of the ATR cell, dried, and rehydrated with an aerosol based on N_2 and 10 mM TRIS-HCl buffer pH 8 (duration: 10 min). After each experiment, cells were carefully re-suspended in 3 x 3 µL LB-amp medium and diluted to 200 µL. This suspension was diluted by a factor of 10^{-5}, spread onto on LB-amp agar plates and incubated at 37°C for 24 h **(A)** or 12 h **(B)**. The figure shows LB-amp agar plates for 200 µL diluted cell cultures (I) – (III). Plate (I) serves as reference (100% growth efficiency or "fitness"). **(A)** Comparing plate (I) and (II) suggests slightly diminished growth of cell cultures that were kept under dry N_2 for 60 min (~90% fitness). **(B)** Comparing plate (I) and (III) suggests slightly diminished growth of cell cultures that were kept under hydrated conditions for 10 min (~80 % viability).

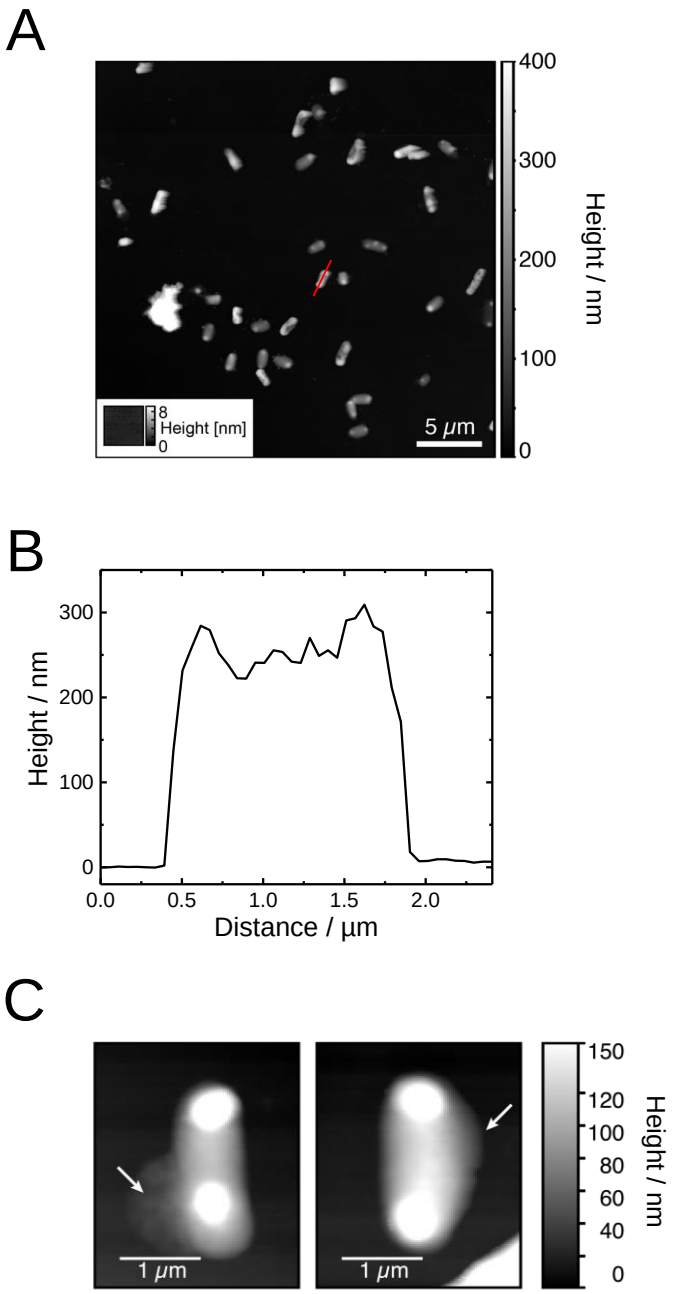

Figure S5. AFM topography of *E. coli* cell suspension dried on template-stripped gold.

(A) AFM height profile of *E. coli* suspension diluted 1:20000 in deionized water and dried on template-stripped gold. Inset: 3x3 µm^2 region of a freshly cleaved, clean template-stripped gold surface. **(B)** Cross-section of a cell (along the red line in (A)). **(C)** Representative AFM topographies of damaged cells. Typically, two out of the seven cells (~30%) that were investigated in detail showed morphological alteration (e.g. protuberances, indicated by arrow). These cells might be considered as partially disintegrated with defects in the cell membrane.

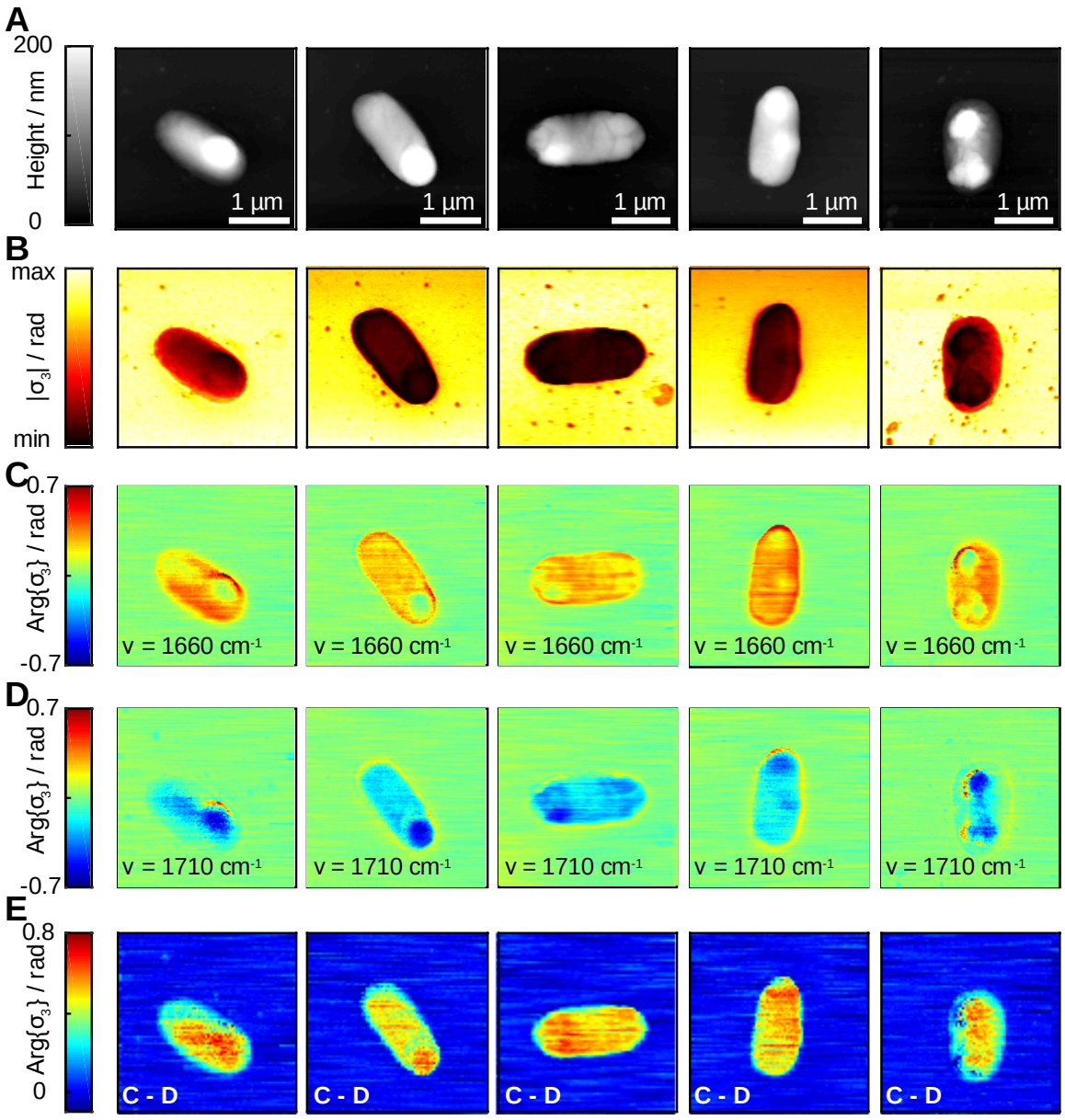

Figure S6. Near-field imaging of five representative *E. coli* cells.

(A) AFM topographies as in Fig. S5. **(B)** *s*SNOM near-field amplitude ($|\sigma_3|$, n=3) maps recorded at 1660 cm^{-1}. **(C)** *s*SNOM near-field phase ($Arg\{\sigma_3\}$, n=3) maps recorded at 1660 cm^{-1}. The phase is sensitive to near-field absorption of the amide I mode of proteins but might be affected by the samples' topography.[4, 5] **(D)** *s*SNOM near-field phase ($Arg\{\sigma_3\}$, n=3) maps recorded at 1710 cm^{-1}. No major absorption band contributes to the phase at this frequency. Only the topography artifact is displayed. As sSNOM predominantly probes the surface of cells we speculate that this may be related to the C=O ester vibration of lipids in the outer *E. coli* membrane.[6] **(E)** Subtraction of the phase maps shown in (C) and (D). No major protein content outside the cells is visible. All phase maps were aligned according to their topography prior to subtraction.

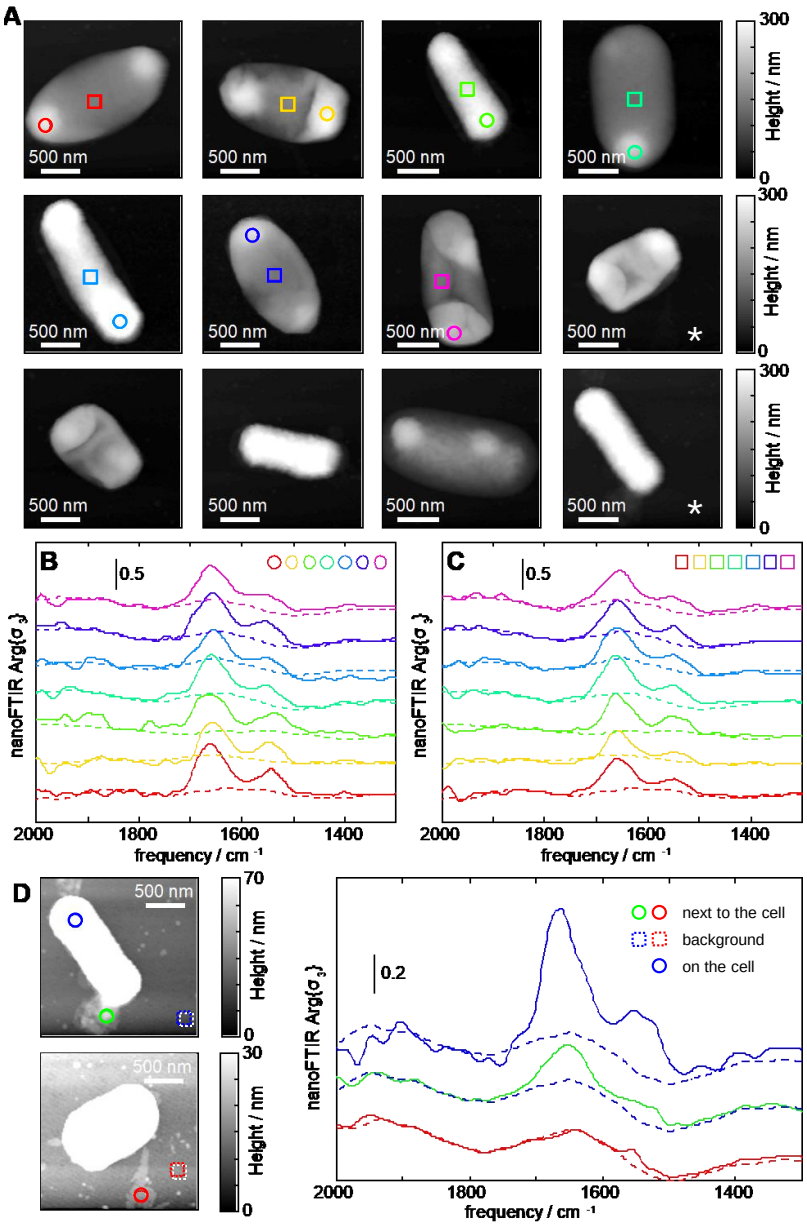

Figure S7. Analysis of further cells by AFM and nanoFTIR.

(A) 12 Topographies of *E. coli* containing overexpressed HydA1. The cells were diluted by 1:20000 in pure H_2O, spread on template stripped gold, and dried under ambient conditions. The field of view (2x2 μm^2) and color scale is identical for all data set. **(B) & (C)** Unreferenced nanoFTIR phase Arg{σ_3} spectra (demodulated at the third harmonic of the tip frequency) recorded at the positions indicated by the colored circles (B, high features) or squares (C, lower features). The dashed lines represent reference spectra recorded next to each cell. All spectra are subject to a linear baseline and an offset. **(D)** Two selected topographies from panel A (lower right column, see asterisk) with a different height scale emphasizing subtle features next to the cell (green and red circle) and on the cell (blue circle). Colored dashed squares: background (template stripped gold). The right panel depicts unreferenced nanoFTIR phase Arg{σ_3} spectra at the positions indicated by the colored circles. The data show that these features may comprise of background artifacts (red trace) or protein (green trace, e.g. from disintegrated cells). The blue trace is for comparison with panels B and C. Dashed traces represent a "clean" background.

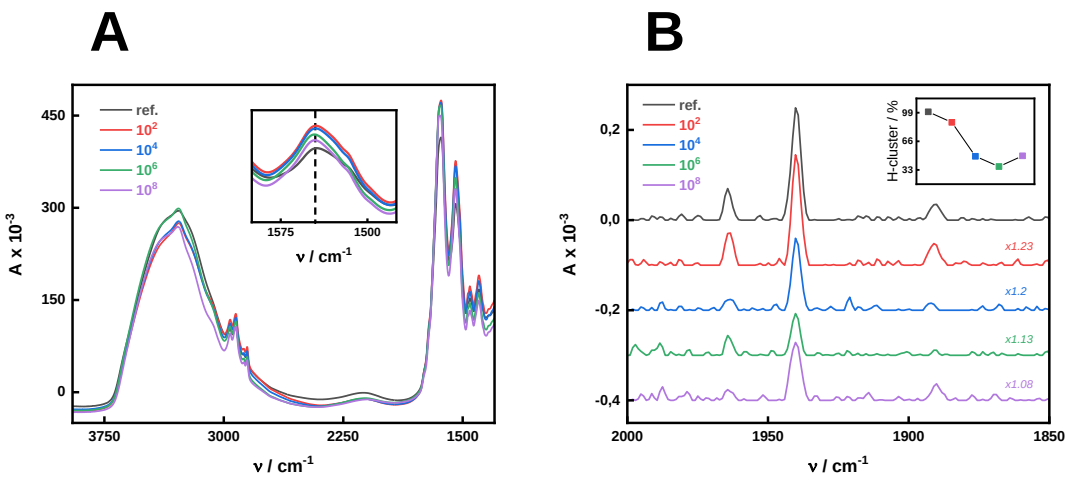

Figure S8. FTIR verification that the activated hydrogenase is located within the cells.

To probe whether recombinant *E. coli* cells eject the heterologously synthesized and activated HydA1 enzyme, cells were washed four times. For this, 1 mL standard cell culture was pelleted at 3000 rpm for 5 minutes. The supernatant was removed and the pellet was suspended in ~10 µL 10 mM TRIS-HCl buffer (pH 8). Then, 1 µL of this suspension was analyzed by ATR FTIR spectroscopy as described in the main text. The remaining suspension was diluted by a factor of 100 with fresh medium (= 1 mL) and pelleted again.

(A) FTIR spectra of rehydrated cell suspensions of wash steps 1 – 5, corresponding to relative volumes of fresh medium between 10^2 and 10^8. Comparing the amide II signal intensity at 1545 cm^{-1} (inset) allows estimating the overall protein concentration. **(B)** Baseline-corrected FTIR spectra in the CO regime of the H-cluster, weighted for the amide II signal intensity differences detected in panel (A). The inset depicted the H-cluster signal intensity (H_{ox} + H_{red}) relative to the undiluted reference sample (= 100%). We observed ~50% stability of hydrogenase in *E. coli* cells that were washed in up to 10^8 times their volume, which suggest only insignificant secretion of hydrogenase enzyme into the medium. The H-cluster signals decrease may be related to osmotic shock and cell lysis (compare Fig. S4). Notably, there is no loss of H-cluster intensity in the first step of dilution.

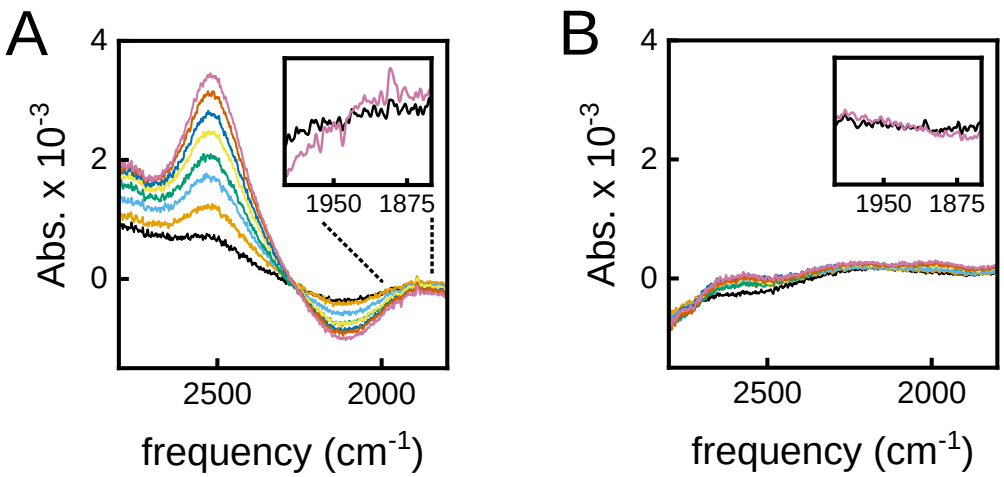

Figure S9. D_2 oxidation activity is specific for [2Fe]^{adt}-HydA1 containing cells.

(A) ATR FTIR difference spectra of [2Fe]^{adt}-HydA1 containing *E. coli* cells indicated an HDO band increase at 2515 cm^{-1} in the presence of D_2 (~100 mbar, exposure time 0 s – 90 s increasing from black to purple). **Inset:** A simultaneous enrichment of H_{red} (1891 cm^{-1}) over H_{ox} (1940 cm^{-1}) was observed. **(B)** In similar experiments, no such changes were observed in *E. coli* cells expressing HydA1 apo-protein in the absence of [2Fe]^{adt} addition.

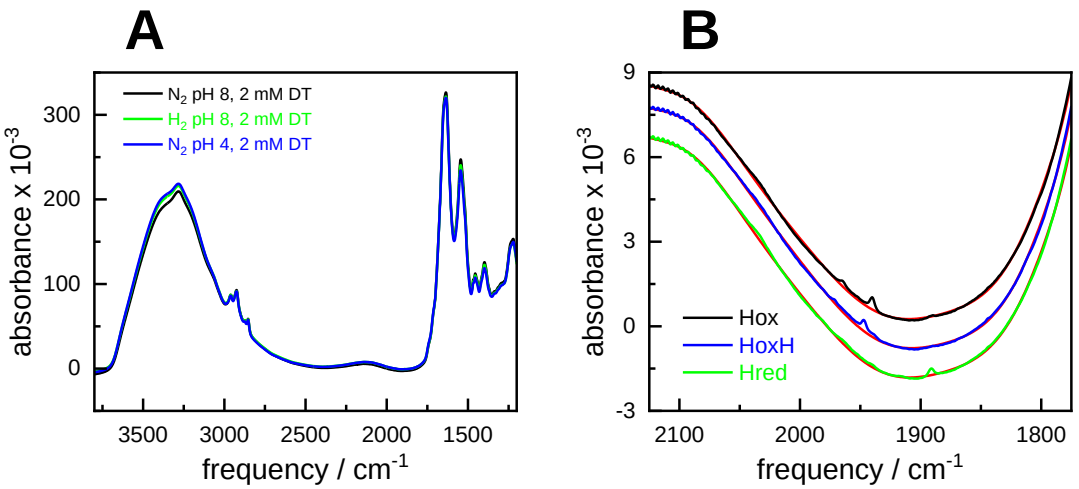

Figure S10. Absolute FTIR spectra as a function of pH and H_2.

(A) Absorbance spectra of samples of *E. coli* cells containing [2Fe]^{adt}-HydA1 exposed to different gas atmospheres (N_2, H_2) at pH 8 and pH 4 (always in the presence of 2 mM dithionite). Hydration level and protein content are comparable under these conditions.
(B) Zoom in of the CO/CN^- ligand regime of HydA1. CO ligand bands were well observable in absolute spectra (in particular the labelled marker bands) whereas the weakly absorbing CN^- ligands were found to be overlaid by instrumental noise. Red traces depict the baseline contribution of liquid water.

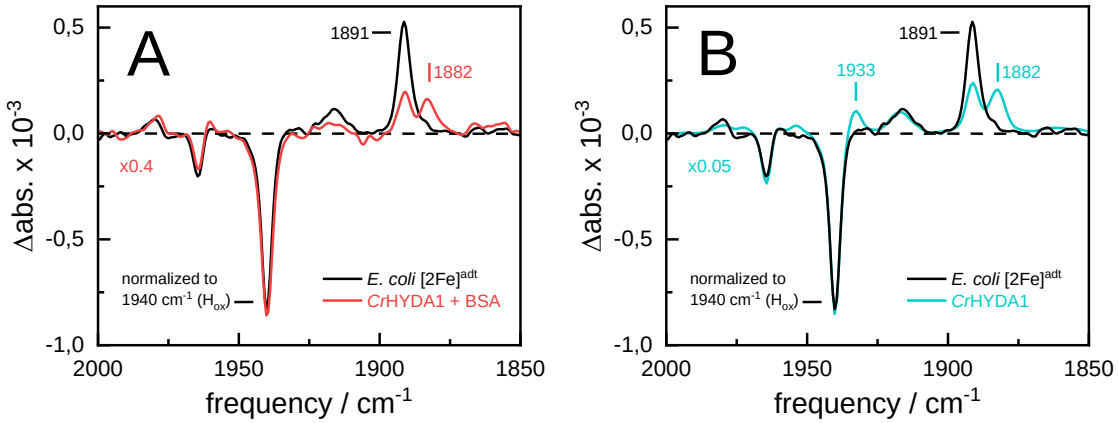

Figure S11. Reactivity differences between purified and whole-cell samples of [2Fe]^{adt}-HydA1 monitored by FTIR spectroscopy.

(A) Purified [2Fe]^{adt}-HydA1 enzyme was diluted with BSA (bovine serum albumin) as an unreactive protein standard to obtain a protein / hydrogenase ratio comparable to *E. coli* cells containing [2Fe]^{adt}-HydA1. Exposed to 100% H_2, both H_{red} (CO marker bands at 1891 cm^{-1}) and H_{sred} (1882 cm^{-1}) are populated in the diluted, purified enzyme sample (red spectrum) whereas only H_{red} is visible in *E. coli* cells (black spectrum). H_{red}´ is not expected to be enriched under these conditions.[7] **(B)** Comparison of undiluted enzyme (blue spectrum) with *E. coli* cells containing [2Fe]^{adt}-HydA1. Here, co-accumulation of H_{red}´ is clearly observed (1933 cm^{-1}).

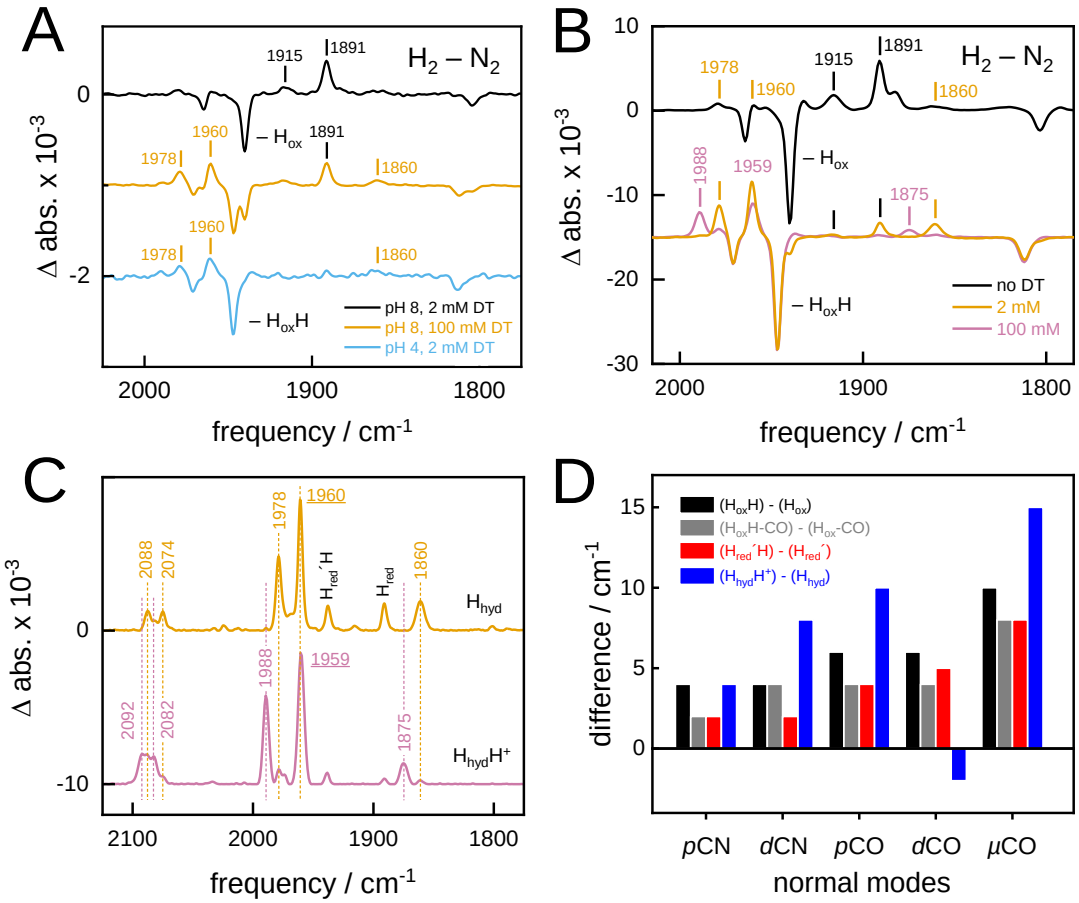

Figure S12. Influence of pH and reductant on the formation of H_{hyd} and $H_{hyd}H^+$ monitored by FTIR spectroscopy.

(A) *In vivo* H_2-N_2 difference spectra for various pH values and dithionite (NaDT) concentrations. Formation of H_{red} (1915 and 1891 cm^{-1}) and depopulation of H_{ox} (1940 cm^{-1}) is observed at pH 8 and 2 mM NaDT (black difference spectrum). Formation of H_{red} and H_{hyd} (1978, 1960 and 1860 cm^{-1}) with depopulation of H_{ox} and $H_{ox}H$ (1946 cm^{-1}) is observed at pH 8 and 100 mM NaDT (dark yellow difference spectrum). Formation of H_{hyd} and depopulation of $H_{ox}H$ is observed at pH 4 and 2 mM NaDT (light blue difference spectrum). This data show how high NaDT concentrations can compensate for high pH values in the enrichment of H_{hyd}, at least partly.

(B) At pH 4 and in the strict absence of NaDT, purified $[2Fe]^{adt}$-HydA1 adopts a mixture of reduced states under 1% H_2. The black trace shows the corresponding H_2 – N_2 difference spectrum. Negative bands are assigned to H_{ox}, positive bands include H_{red} (black labels), H_{hyd} (dark yellow labels), and traces of H_{red}´ and H_{sred} (not annotated). At pH 4 and in the presence of ~2 mM NaDT, purified $[2Fe]^{adt}$-HydA1 converts from $H_{ox}H$ into H_{hyd} with a small percentage of Hred (dark yellow trace), as previously reported.[8] At pH 4 and in the presence of ~100 mM NaDT, purified $[2Fe]^{adt}$-HydA1 converts from $H_{ox}H$ into $H_{hyd}H^+$ (pink trace). This species was observed in $[2Fe]^{adt}$-HydA1 C169S previously.[9]

(C) Careful subtraction of $H_{ox}H$ from the dark yellow and pink traces in (B) allows the generation of relatively pure spectra of H_{hyd} and $H_{hyd}H^+$, respectively (contributions by Hred and $H_{red}´H$ are indicated). While most bands are strongly shifted towards higher wavenumbers in $H_{hyd}H^+$ relative to H_{hyd}, we found no significant difference between the (putative) dCO band at 1960 cm^{-1} (H_{hyd}) and 1959 cm^{-1} (H_{hyd}H+), this specific peak assignment is in contrast to an earlier assignment of the proposed $H_{hyd}H^+$ state.[9]

(D) Subtraction of vibrational frequencies of CO/CN^- normal modes for H_{ox}, H_{ox}-CO, $H_{red}´$, and their protonated counterparts $H_{ox}H$, $H_{ox}H$-CO, and $H_{red}´H$ (compare Table S2). The coupled δ-mode of H_{ox}-CO is excluded. Index p (proximal) and d (distal) refers to the relative position of the Fe ion to the $[4Fe\text{-}4S]_H$ cluster. Index μ marks the Fe-Fe bridging CO ligand. The mean differences are ~3 cm^{-1} for p/dCN, ~5 cm^{-1} for p/dCO, and ~9 cm^{-1} for μCO. These shifts have been attributed to a protonation of the [4Fe-4S] cluster.[7] In comparison, the differences between the hydride states (blue bars) are significantly larger (or smaller, i.e. for dCO). This observation inspired our decision to assign the blue-shifted IR signature of H_{hyd} to a hydride-binding H-cluster geometry with a protonated adt ligand, $H_{hyd}H^+$. A similar assignment was suggest by Mulder et al. previously.[9]

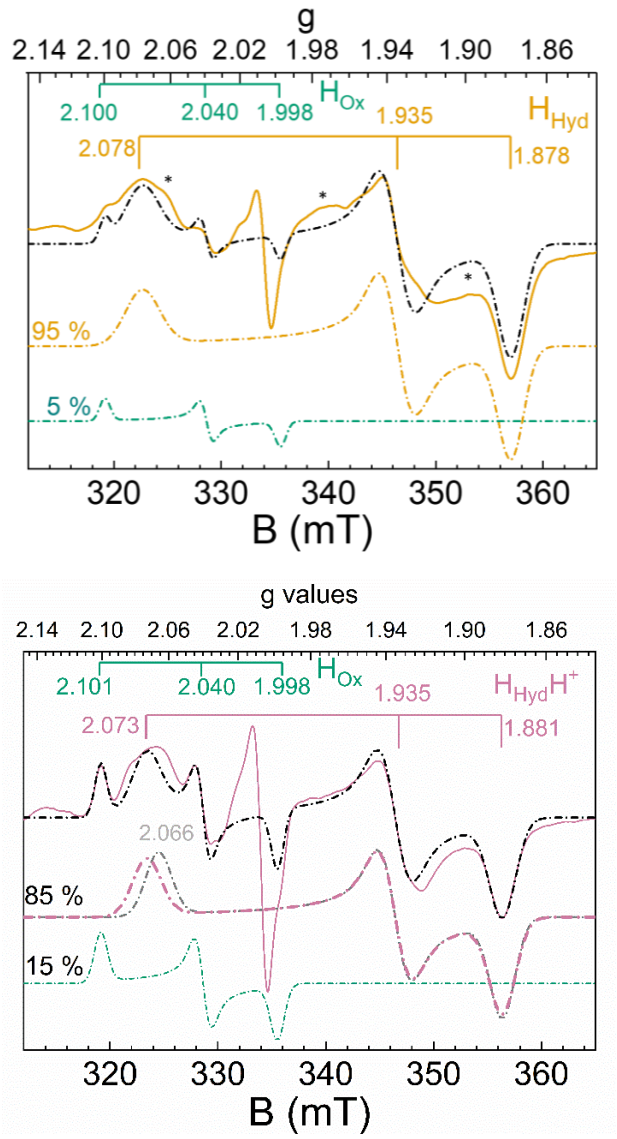

Figure S13. Simulation details of EPR spectra recorded at 20 K showing two hydride-like states detected at high and low pH.

(Top panel): High pH EPR spectrum (dark yellow solid line) simulated as a combination of H_{ox} (cyan dash-dotted line) and H_{hyd} (dash-dotted dark yellow line). Potential contributions from the previously reported "rhombic 2.06 signal" indicated with asterisks (reported g = 2.061, 1.968, 1.900).[9, 10] Previously reported g-values for the "rhombic 2.08 signal" assigned to the H_{hyd} state: 2.078; 1.935; 1.880.[9-11] **(Bottom panel)**: Low pH EPR spectrum (purple solid line) simulated as a combination of $H_{ox}H$ (cyan dash-dotted line) and $H_{hyd}H^+$ (purple dash-dotted line), also shown is a simulation highlighting an additional feature at g = 2.066 visible at low microwave power.

In both spectra the low field region is complex suggesting the presence of additional minor species, however, at high microwave power these contributions become negligible (Fig. S14). Contributions from H_{sred} are unlikely due to the absence of the expected high field feature at g = 1.868,[12] see also Fig. S10. The final simulations are shown as black dash-dotted lines. The hydride species are generated under H_2 atmosphere in the presence of 10 mM NaDT, experimental parameters as in main text Fig. 5.

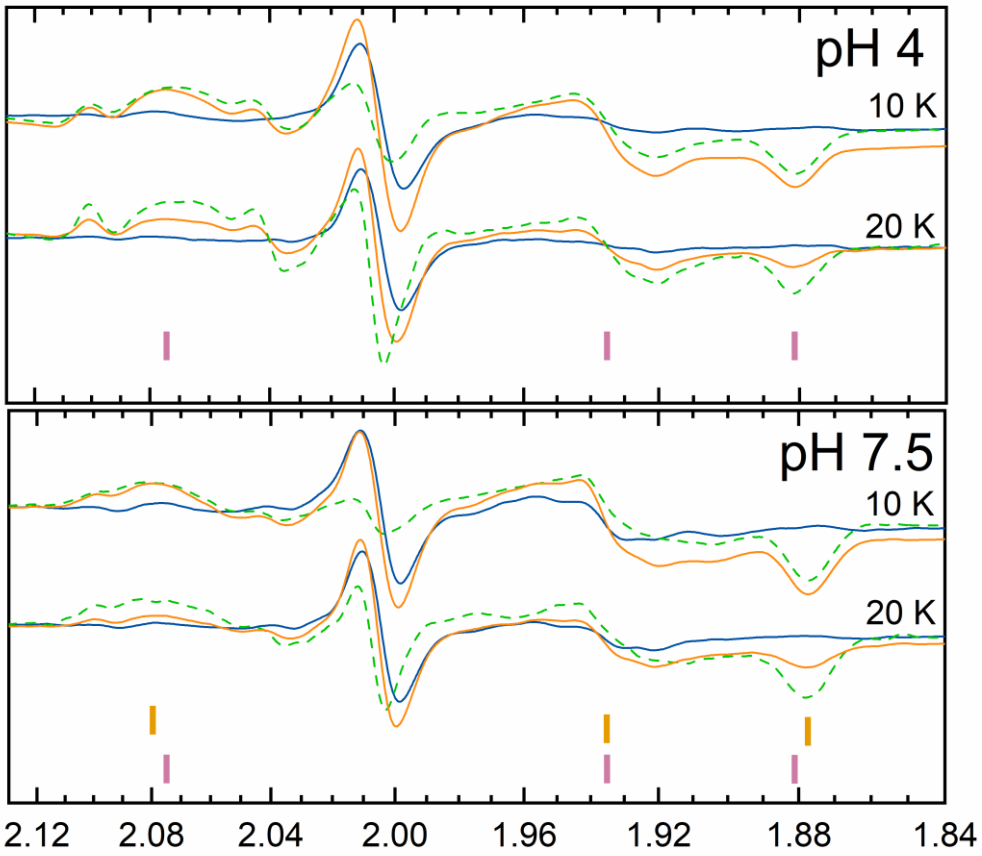

Figure S14. Temperature effects on the EPR signals attributed to hydride states detected at low and high pH.

Upper panel (pH 4): EPR spectra recorded at 10 K (top lane) and 20 K (bottom lane) of *E. coli* cells in pH 4 TRIS-HCl media (100 mM TRIS, 150 mM NaCl) containing apo-HydA1 (blue spectra) and $[2Fe]^{adt}$-HydA1 (orange spectra); also shown are the background subtracted spectra of $[2Fe]^{adt}$-HydA1 (green dashed lines).

Lower panel (pH 7.5): EPR spectra recorded at 10 K (top lane) and 20 K (bottom lane) of *E. coli* cells in pH 7.5 TRIS-HCl media (100 mM TRIS, 150 mM NaCl) containing apo-HydA1 (blue spectra) and $[2Fe]^{adt}$-HydA1 (orange spectra); also shown are the background subtracted spectra of $[2Fe]^{adt}$-HydA1 (green dashed lines).

The background corrected spectra are normalized at the g_z through to facilitate comparison. The g-values for $H_{hyd}H^+$ (2.073, 1.935 and 1.881, purple vertical lines) and H_{hyd} (2.079, 1.935 and 1.878, yellow vertical lines) are indicated for clarity. Spectra recorded at 10 and 20 K reveal only negligible temperature induced differences in the signals attributed to H_{hyd} and $H_{hyd}H^+$. Spectra recorded at 10 μW, other experimental parameters as in Figure 5.

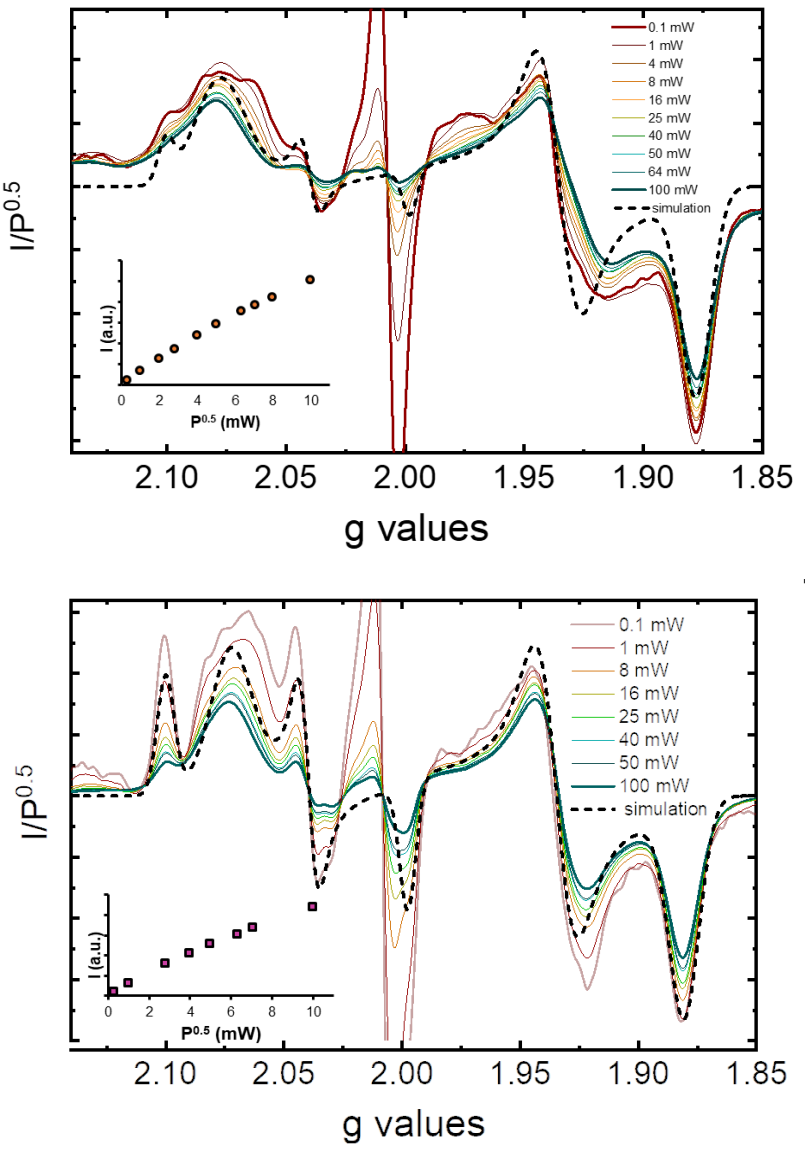

Figure S15. Power dependence of the hydride states detected at high and low pH monitored at 20 K.

Both the H_{hyd} (**top**) and $H_{hyd}H^+$ (**bottom**) signal increase as a function of microwave power and neither signal saturates rapidly at 20 K, in good agreement with the behavior reported at 20 K for the "rhombic g = 2.08" signal previously assigned to the H_{hyd} state.[9-11] Insets show power saturation plots (I vs $P^{0.5}$) of the H_{hyd} (orange circles) or $H_{hyd}H^+$ (purple squares) signals. The signal intensity plotted in the insets is determined from their respective g_x component, as this is the most isolated part of the signal. Plots of the g_z and g_y components yield similar saturation behavior. The signal displayed only limited saturation within the available experimental window (microwave power, $P \leq 100$ mW), underscoring the fast relaxing nature of the species. The g-values are obtained from simulations (see Fig. S13) and the respective simulated spectra are redrawn from Figure 5 for clarity (black dashed lines). It is noteworthy that in particular the low field tensor becomes more distinct at higher power, albeit the exact g-values are potentially slightly shifted due to power saturation. The hydride species are generated under H_2 atmosphere in the presence of 10 mM NaDT, microwave power indicated in figure, and spectra shown without background subtraction, other experimental parameters as in main text Figure 5.

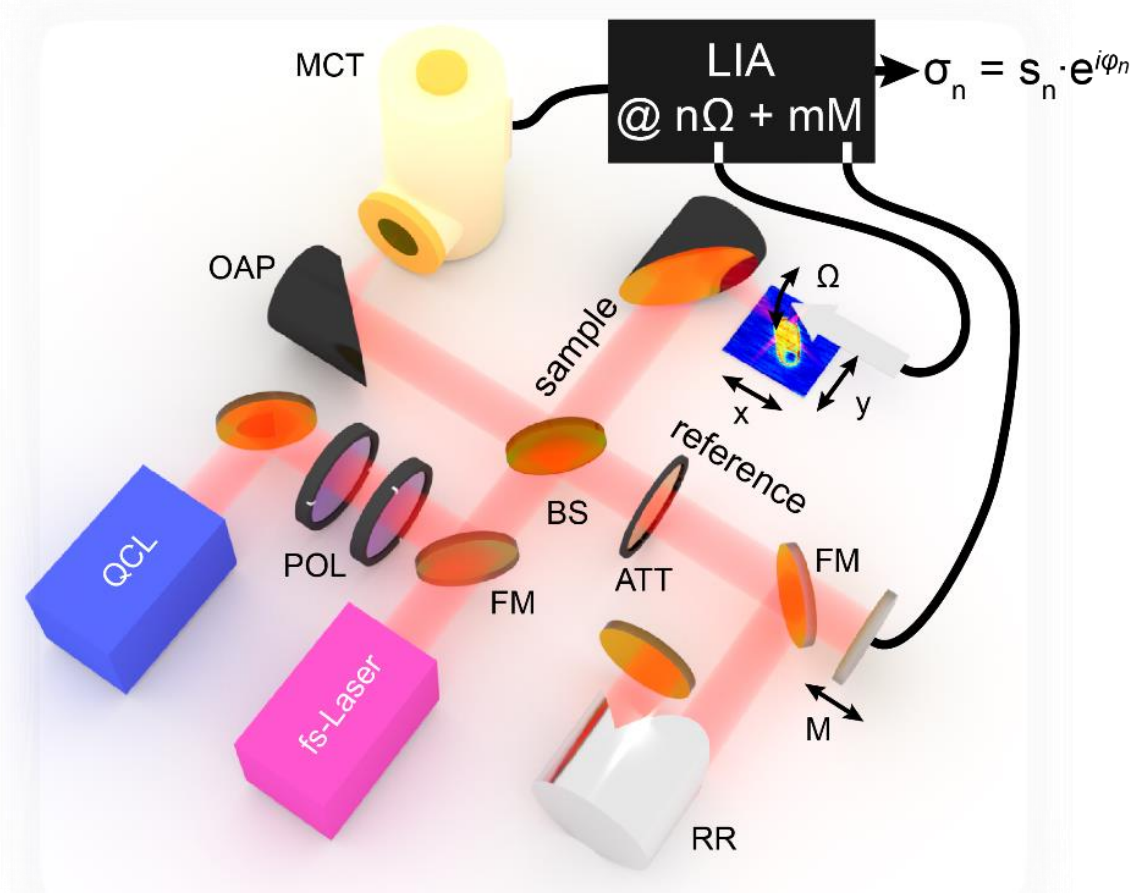

Figure S16. sSNOM and nanoFTIR setup.

The light of either a quantum-cascade laser (QCL, attenuated by a pair of polarizers, POL) or fiber-based fs laser system (selectable by a flip mirror, FM) is focused by an off-axis parabolic mirror (OAP) on the tip of an atomic force microscope (AFM). The scattered light interferes with phase-modulated light from a reference arm (attenuated by a gold grid attenuator, ATT) at a ZnSe beam-splitter (BS) and is detected by a mercury-cadmium-telluride detector (MCT) and demodulated by a lock-in amplifier (LIA). For nanoFTIR the light in the reference arm travels through a retroreflector (RR) and is back-reflected by a folding mirror.

AFM topographies were recorded on a commercial AFM (NanoWizard II, JPK Instruments AG, Germany) with a Pt coated cantilever (Arrow NCPt, NanoWorld GmbH, Germany) in intermittent contact mode under ambient conditions.

The scattering-type scanning near-field optical microscope (sSNOM) is conceptually setup as described above.[13] Either a quantum-cascade laser (Daylight Solutions, USA) or fiber-based fs-laser system (NeaSpec GmbH, Germany) is focused by an off-axis parabolic mirror onto a metalized AFM tip (Arrow NCPt, NanoWorld GmbH, Germany) oscillating close to its first mechanical resonance Ω. The scattered light is collected by the same mirror and is directed by a beam-splitter (ZnSe plate, Ø25.4, thickness 3 mm, Eksma Optics, Lithuania) towards a mercury-cadmium-telluride detector (KLD-0.1-J1/11/DC, Kolmar Technologies, Inc., USA). There the scattered light interferes with light from the reference arm whose optical path difference is modulated by the mirror mounted on a piezo actuator (P-843.10, Physik

Instrumente (PI) GmbH & Co. KG, Germany) sinusoidally displacing it at a frequency of M ~ 300 Hz. The doubly modulated signal is then demodulated by a lock-in amplifier (HF2LI, Zurich Instruments, Switzerland) at the frequencies nΩ ± mM similar as described in ref. 13 and registered while the sample is being moved in x-y plane underneath the AFM tip. The demodulated maps are then phase corrected as described in ref. 14. Additionally, a constant phase is subtracted line-by-line such that the phase at the maximal amplitude in each line equals to zero. Two maps were recorded per cell: one at 1660 cm^{-1} (Fig. S6) displaying the amide I contribution and potential topography artifacts and one at 1710 cm^{-1} (Fig. S6) which is only affected by the topography artifact. Those artifacts may be related to differences in illumination or loading of the antenna while scanning across the sample.[4, 5] The map recorded at 1710 cm^{-1} was then subtracted from the map at 1660 cm^{-1}.

For broadband nano-Fourier transform infrared (nanoFTIR) spectroscopy[15] the broadband fs-laser source is selected via the flip mirror. The optical path in the reference arm is changed such that the light is reflected off a retroreflector mounted on a voice-coil stage (V-524, Physik Instrumente (PI) GmbH & Co. KG, Germany) and being folded back by a folding mirror. While the tip sits on a specific location on the sample the reference mirror is periodically driven 0.4 mm with a velocity 0.05 mm/s. The relative position of the reference mirror is determined by an auxiliary HeNe-laser Michaelson interferometer. Both, IR and HeNe interferograms are simultaneously recorded by the LIA and stored (for the IR interferogram only the demodulated signal at n=1, 2 and 3 is recorded). The IR interferogram is sampled at the zero-crossings of the HeNe interferogram and saved. Such treated interferograms are first aligned relative to their white light position by cross-correlation during post processing. All spectra are apodized by a 4-term Blackman-Harris apodization function resulting in spectra with a spectral resolution of $\Delta\nu \sim 16$ cm^{-1}. All spectra were phase corrected by a Mertz-type phase correction to compensate for slowly varying phase changes. During the phase correction a spectrally low-resolution ($\Delta\nu \sim 658$ cm^{-1}) phase spectrum was generated by applying a 12 point wide 4-term Blackman-Harris apodization before Fourier-transform. This low-resolution phase spectrum was then subtracted from the phase of the high-resolution spectrum. This allowed us to display the near-field phase spectra of *E. coli* cells and the template-stripped gold substrate separately (Figure 3 in main text) without referencing it to a reference spectrum as typically done in near-field spectroscopy.[13-15]

Supporting Tables

Table S1: CO band frequencies of the H-cluster in HydA1 as observed *in vivo*.
The CN^- frequencies were not resolved at sufficient signal-to-noise.

	*ν*CO / cm^{-1}		
H_{ox}	1964	1940	1802
$H_{ox}H$	1970	1946	1812
H_{red}'	n.d.	n.d.	n.d.
$H_{red}'H$	n.d.	n.d.	n.d.
H_{hyd}	1978	1960	1860
$H_{hyd}H^+$	1988	1959	1875
H_{red}	1961	1915	1891
H_{sred}	n.d.	n.d.	n.d.
H_{ox}-CO	1968	1962*	1808
$H_{ox}H$-CO	n.d.	n.d.	n.d.

* In the CO-inhibited state, the coupled pCO/ dCO stretching vibration gives rise to an additional IR band at 2012 cm^{-1} (H_{ox}-CO); n.d. = not detected. (Note: H_{red}' and H_{red} are in some reports also referred to as H_{red} and $H_{red}H^+$, respectively)

Table S2: CO/CN^- band frequencies of the H-cluster in HydA1 as observed *in vitro*. Data taken from reference [7].

	νCN^- / cm^{-1}		νCO / cm^{-1}		
H_{ox}	2088	2070	1964	1940	1802
$H_{ox}H$	2092	2074	1970	1946	1812
H_{red}'	2084	2066	1962	1933	1792
$H_{red}'H$	2086	2968	1966	1938	1800
H_{hyd}	2088	2074	1978	1960	1860
$H_{hyd}H^+$	2092	2082	1988	1959	1875
H_{red}	2070	2033	1961	1915	1891
H_{sred}	2068	2026	1953	1918	1882
H_{ox}-CO	2092	2082	1968	1962*	1808
$H_{ox}H$-CO	2094	2086	1972	1966*	1816

* In the CO-inhibited state, the coupled pCO/ dCO stretching vibration gives rise to an additional IR bands at 2012 cm^{-1} (H_{ox}-CO) and 2006 cm^{-1} ($H_{ox}H$-CO). (Note: H_{red}' and H_{red} are in some reports also referred to as H_{red} and $H_{red}H^+$, respectively)

Table S3: g-values of selected states reported for the H-cluster in HydA1

Species	**gz**	**gy**	**gx**	**reference**
H_{ox}	2.100-2.101	2.04	1.998	16 and this work
H_{ox}-CO	2.054	2.007	2.007	15
H_{sred}	2.076	1.943	1.868	12
H_{hyd}	2.077-8	1.935	1.880	9-11
H_{hyd}	2.078	1.935	1.878	this work
$H_{hyd}H^+$	2.073	1.935	1.881	this work

References

1. N. Khanna, C. Esmieu, L. S. Meszaros, P. Lindblad and G. Berggren, *Energy Environ. Sci.*, 2017, **10**, 1563-1567.
2. J. Esselborn, C. Lambertz, A. Adamska-Venkatesh, T. Simmons, G. Berggren, J. Noth, J. Siebel, A. Hemschemeier, V. Artero, E. Reijerse, M. Fontecave, W. Lubitz and T. Happe, *Nat Chem Biol*, 2013, **9**, 607-609.
3. J. W. Foster, *Nat. Rev. Microbiol.*, 2004, **2**, 898-907.
4. E. Yoxall, M. Schnell, S. Mastel and R. Hillenbrand, *Opt. Express*, 2015, **23**, 13358-13369.
5. P. S. Carney, B. Deutsch, A. A. Govyadinov and R. Hillenbrand, *ACS Nano*, 2012, **6**, 8-12.
6. S. C. Edington, J. C. Flanagan and C. R. Baiz, *The Journal of Physical Chemistry A*, 2016, **120**, 3888-3896.
7. M. Senger, S. Mebs, J. Duan, O. Shulenina, K. Laun, L. Kertess, F. Wittkamp, U.-P. Apfel, T. Happe, M. Winkler, M. Haumann and S. T. Stripp, *Phys. Chem. Chem. Phys.*, 2018, **20**, 3128-3140.
8. M. Winkler, M. Senger, J. Duan, J. Esselborn, F. Wittkamp, E. Hofmann, U.-P. Apfel, S. T. Stripp and T. Happe, *Nat. Comm.*, 2017, **8**, 16115.
9. D. W. Mulder, M. W. Ratzloff, M. Bruschi, C. Greco, E. Koonce, J. W. Peters and P. W. King, *J. Am. Chem. Soc.*, 2014, **136**, 15394-15402.
10. D. W. Mulder, M. W. Ratzloff, E. M. Shepard, A. S. Byer, S. M. Noone, J. W. Peters, J. B. Broderick and P. W. King, *J. Am. Chem. Soc.*, 2013, **135**, 6921-6929.
11. D. W. Mulder, Y. Guo, M. W. Ratzloff and P. W. King, *J. Am. Chem. Soc.*, 2017, **139**, 83-86.
12. A. Adamska, A. Silakov, C. Lambertz, O. Rüdiger, T. Happe, E. Reijerse and W. Lubitz, *Angew. Chem. Int. Ed.*, 2012, **51**, 11458-11462.
13. N. Ocelic, A. Huber and R. Hillenbrand, *Appl. Phys. Lett.*, 2006, **89**, 101124.
14. C. Moreno, J. Alda, E. Kinzel and G. Boreman, *Appl. Opt.*, 2017, **56**, 1037-1045.
15. F. Huth, A. Govyadinov, S. Amarie, W. Nuansing, F. Keilmann and R. Hillenbrand, *Nano Lett.*, 2012, **12**, 3973-3978.
16. C. Kamp, A. Silakov, M. Winkler, E. J. Reijerse, W. Lubitz and T. Happe, *Biochimica et Biophysica Acta (BBA) - Bioenergetics*, 2008, **1777**, 410-416.